Supporting Information

Carbon-Stabilized Interlayer-Expanded Few-layer $MoSe_2$ Nanosheets for Sodium Ion Batteries with Enhanced Rate Capability and Cycling Performance

Yongchao Tang, Zongbin Zhao, Yuwei Wang, Yanfeng Dong, Yang Liu, Xuzhen Wang and Jieshan Qiu**

State Key Lab of Fine Chemicals, Liaoning Key Lab for Energy Materials and Chemical Engineering, PSU-DUT Joint Center for Energy Research, School of Chemical Engineering, Dalian University of Technology, Dalian 116024, P. R. China

**Corresponding author: Prof. Zongbin Zhao, Prof. Jieshan Qiu*

E-mail: zbzhao@dlut.edu.cn, jqiu@dlut.edu.cn

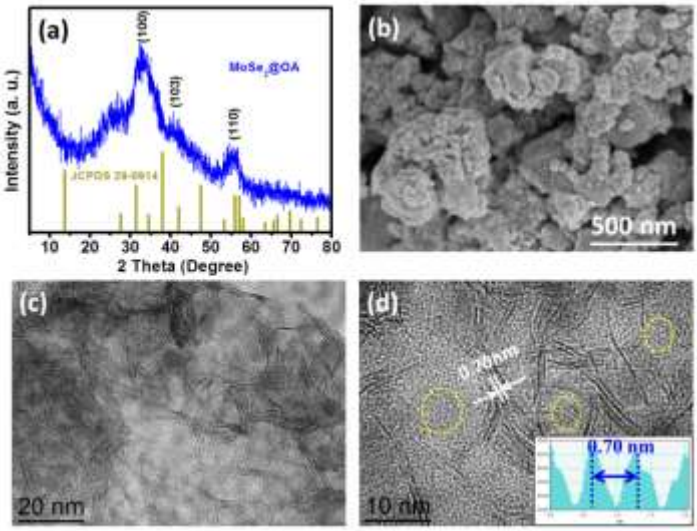

Figure S1. Chemical compositions and morphological features of $MoSe_2$@OA. (a) XRD pattern, (b) FE-SEM image, (c)-(d) HR-TEM images of $MoSe_2$@OA.

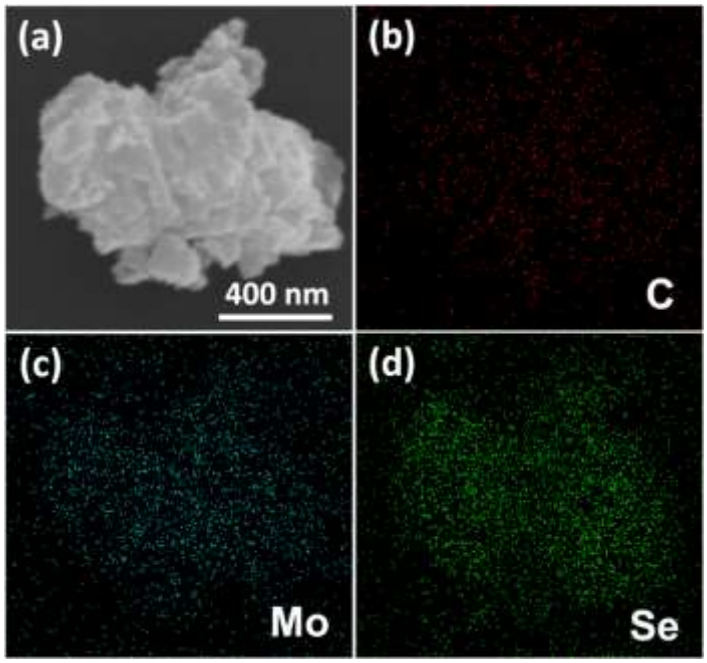

Figure S2. FE-SEM image and EDS element mapping of $MoSe_2$@C. (a) FE-SEM image of $MoSe_2$@C. (b)-(d) EDS elemental mapping including C, Mo, and Se.

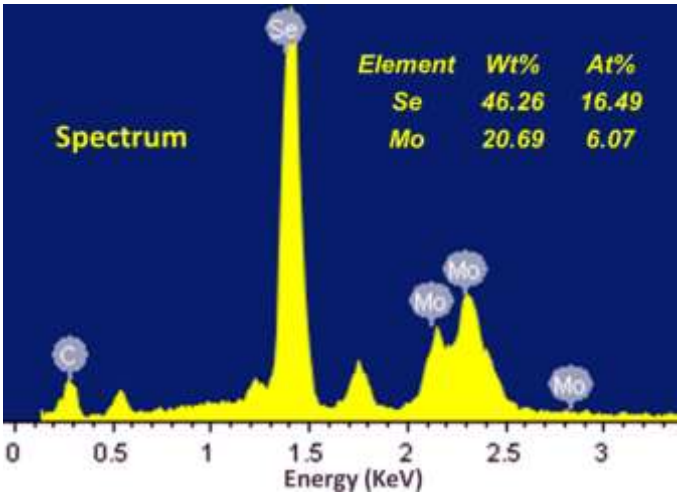

Figure S3. EDS spectrum and element contents of the $MoSe_2$@C. The EDS spectrum of $MoSe_2$@C shows that the atomic ratio of Mo to Se approaches 1 : 2, which is in consistent with the stoichiometric ratio of the $MoSe_2$ compound.

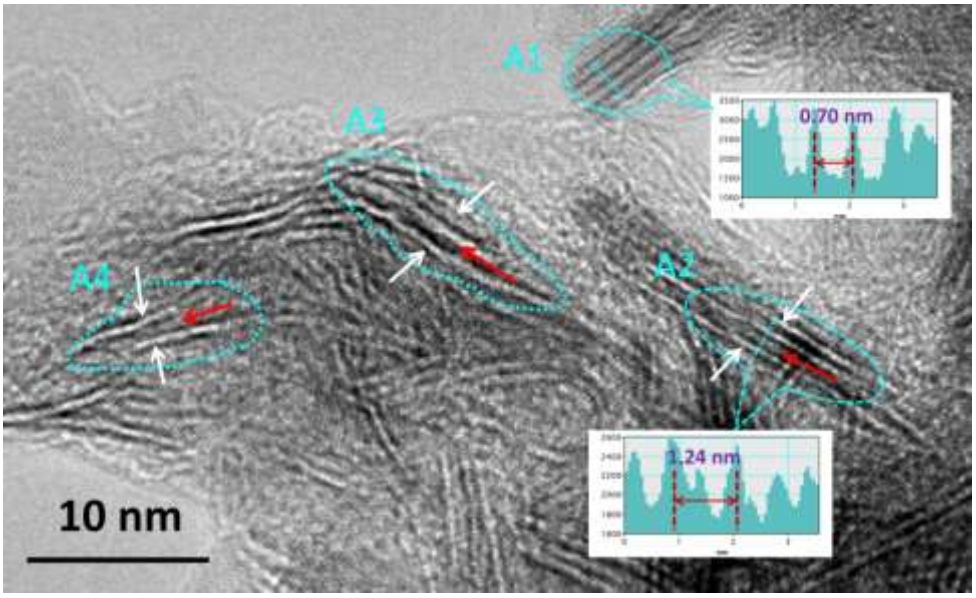

Figure S4. HR-TEM image of $MoSe_2$@C showing the presence of sandwiched carbon layer (pointed in red arrows) by $MoSe_2$ layers (pointed in white arrows).

As shown in **Figure S4**, in A1 region, the $MoSe_2$ exhibits typically interlayer spacing of ca. 0.70 nm, corresponding to the few-layer $MoSe_2$ without sandwiched carbon. By contrast, in A2 region, the interlayer spacing of the $MoSe_2$ increases to ca. 1.24 nm, in which the increased value (0.54 nm) should result from the sandwiched carbon since the value is smaller than the interlayer

spacing (0.7 nm) of the $MoSe_2$. Such results are similar to that reported elsewhere previously.[1] Analogue to the A2 region, the $MoSe_2$ in A3 and A4 regions also show similar results. Based on the abovementioned discussion, the layers (pointed by red arrows) between $MoSe_2$ layers (pointed by white arrows) could be ascribed to the carbon derived from OA-PDA.

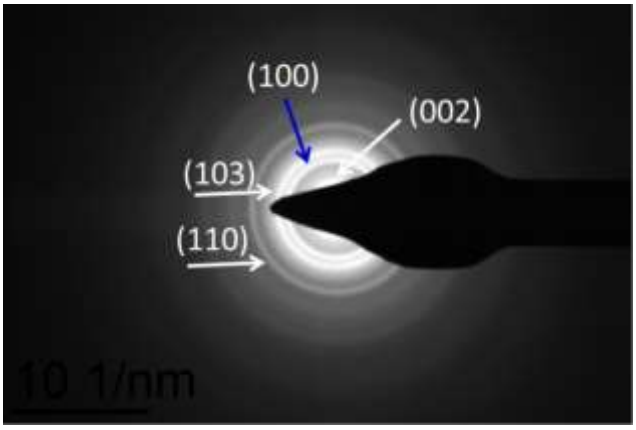

Figure S5. SAED patterns of the $MoSe_2$@C. The selected area electron diffraction (SAED) patterns of the $MoSe_2$@C exhibits well-defined diffraction rings, which can be assigned to (100), (103), (002) and (110) crystal planes, respectively. Such results further suggest the decent crystallinity of $MoSe_2$ in the $MoSe_2$@C.

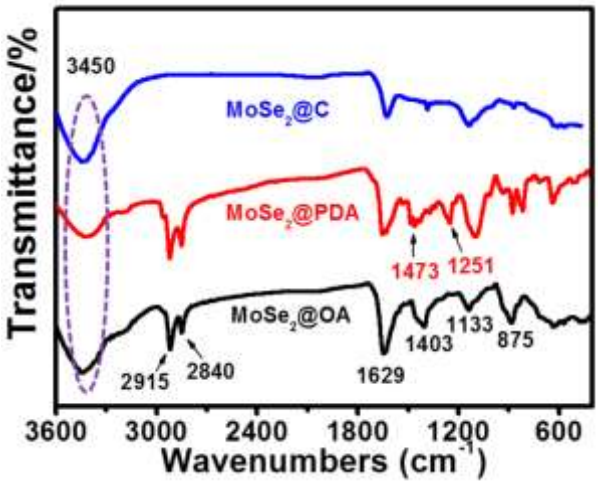

Figure S6. FT-IR spectra of the $MoSe_2$@OA, $MoSe_2$@PDA, and $MoSe_2$@C. In $MoSe_2$@OA, the peaks at 1629, 1403, 1133, 875 cm^{-1} are originated from C=O, O-H, C−O, and C-H bonds of the OA, respectively (the peaks at 3450, 2915, and 2840 cm^{-1} are inherited from H_2O in air, CH_3 and CH_2 in

the OA). By contrast, two newly-appeared peaks at 1473 and 1251 cm^{-1} in the $MoSe_2$@PDA should be derived respectively to benzene ring and C-N bond. After carbonization, the featured peaks of benzene ring and C-N bond are disappeared nearly due to the formation of $MoSe_2$@C.

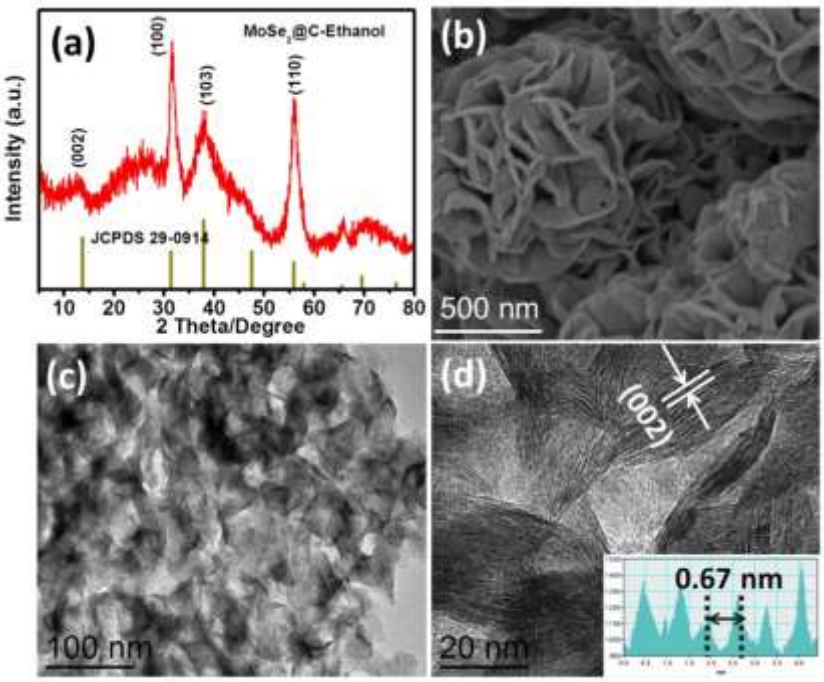

Figure S7. Chemical compositions and morphological characterizations of $MoSe_2$@C-Ethanol. (a) XRD pattern, (b) FE-SEM image, (c)-(d) TEM and HR-TEM images of sample.

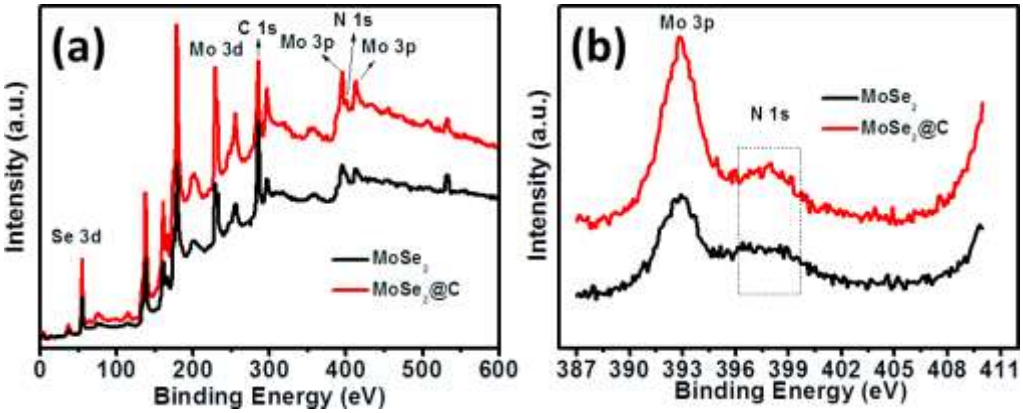

Figure S8. XPS survey scan (a) and high-resolution N 1s spectra (b) comparison of $MoSe_2$ and $MoSe_2$@C.

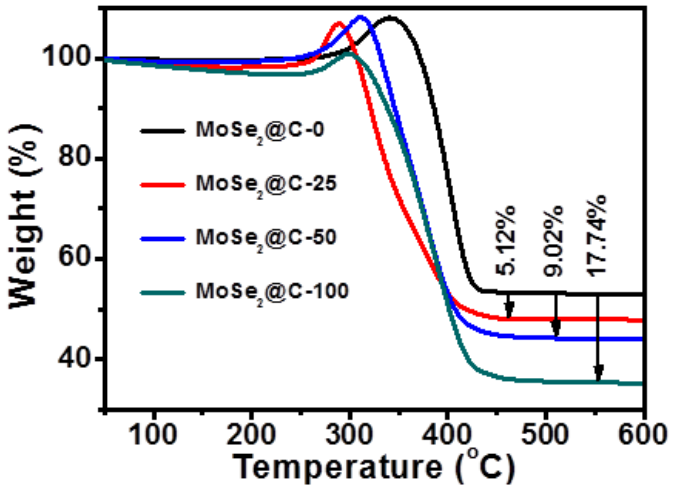

Figure S9. TGA curves of the $MoSe_2$@C composites with different carbon contents. The numbers in the end of the sample name represent the dopamine dosages (0, 25, 50, 100 mg) during the PDA coating, respectively.

As can be seen, the carbon content is typical *ca.* 9.02 wt% in the $MoSe_2$@C, when the dosage of the added dopamine is 50 mg. Herein, the increased weight in 300-350 ^{o}C should be caused by the formation of solid SeO_2 and MoO_3 during the oxidation of the $MoSe_2$@C. Subsequently, the weight loss occurs gradually with the sublimation of the SeO_2 at *ca.* 350 ^{o}C (the sublimation of solid MoO_3 will happen at above 600 ^{o}C) and the combustion of carbon layer.

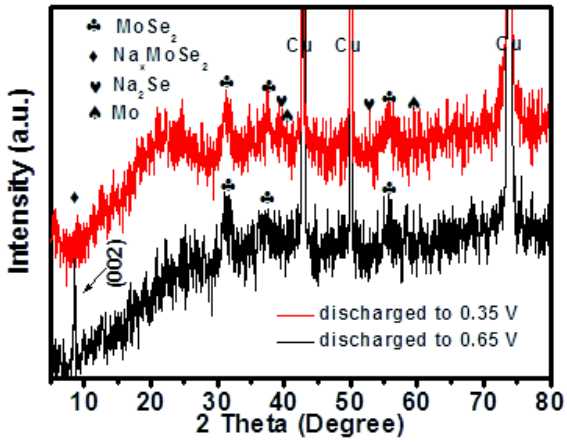

Figure S10. XRD patterns of samples discharged to 0.65 and 0.35 V suggesting the occurrence of intercalation and conversion reaction in the first cycle.

As shown in **Figure S10**, when discharged to 0.65 V, a peak appears at ca. 8.6^{o}, which corresponds to the formation of Na_xMoSe_2, indicating an increased interlayer spacing of (002) lattice plane compared with original (002) lattice plane. Upon sequentially discharged to 0.35 V, the (002) peak disappears with the formation of Mo metal and Na_2Se phases, suggesting the occurrence of conversion reaction.

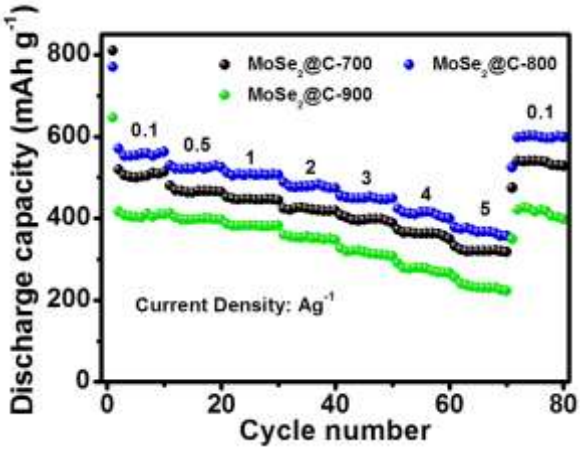

Figure S11. The rate capability test of the $MoSe_2$@C samples from different annealing temperatures. The number in the end of sample name stands for the annealing temperature.

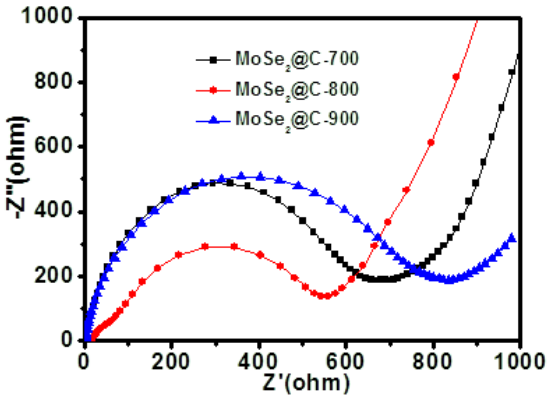

Figure S12. EIS spectra of samples from different annealing temperatures. Compared with other two samples, the sample from 800 ^{o}C presents the smallest semi-cycle and largest-slope tail in middle frequency region and low frequency region, respectively. Such results suggest that the annealing at 800 ^{o}C is advantageous to obtain optimum electronic and ionic conductivity of composite.

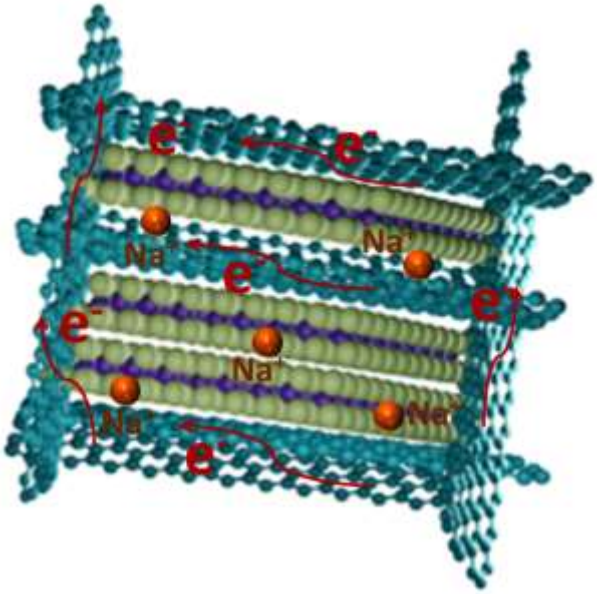

Figure S13. Schematic illustration of ionic and electronic expressway in the $MoSe_2$@C nanosheets. Therein, the carbon layers act as conductive framework and accommodate the volume change from discharge-charge cycling. Moreover, the electrolyte can be allowed to permeate into the inner of $MoSe_2$@C, resulting in an enhanced ionic conductivity.

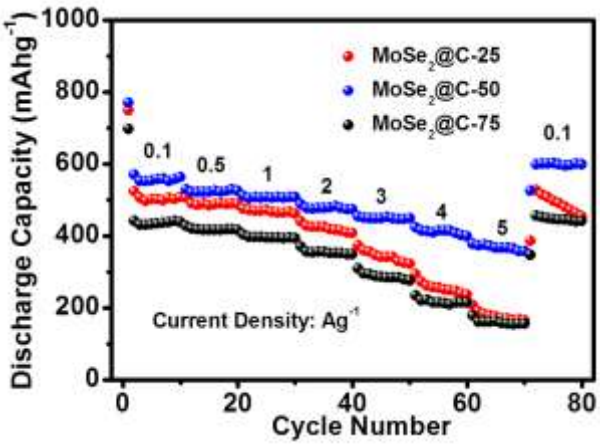

Figure S14. Rate capability test of $MoSe_2$@C with various carbon contents. The numbers in the end of the sample name represent the dopamine dosages (0, 25, 50, 100 mg) during the PDA stabilization, respectively.

Table S1. Rate capability of various reported $MoSe_2$ based anode materials for SIBs.

Current Density (A g^{-1})	$MoSe_2$@C	MoS_2/G [2]	$FeSe_2$ [3]	MoS_2-C [1]	SnS_2 [4]	MoS_2@G [5]	$MoSe_2$@CNTs [6]
	Capacity (mAh g^{-1})	Capacity (mAh g^{-1})	Capacity (mAh g^{-1})	Capacity (mAh g^{-1})	Capacity (mAh g^{-1})	Capacity (mAh g^{-1})	Capacity (mAh g^{-1})
0.04		550					
0.08		500					
0.1	545		450		720		
0.16		450					
0.2		590		475	680		500
0.3					650		
0.32		400					
0.4							
0.5	520	500	400	450	620		450
0.64		350					
0.8		450					440
1	502		390	425	550	420	430
1.5		430					

2	474		390	420		400
3	446				350	
4	411					
7					250	
5	365	370	345			
10		320	295		220	
15		260				
20		220	175			
25		210				

*All the data are excerpted from the corresponding literature.

As can be seen, the $MoSe_2$@C shows a remarkable merit over other anode materials reported elsewhere, especially at larger current densities.

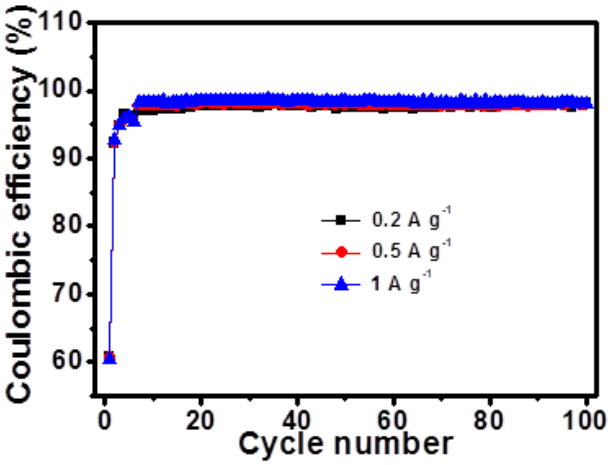

Figure S15. Coulombic efficiencies of $MoSe_2$@C anode material for the SIBs over 100 cycles at various current densities.

All the coulombic efficiencies in 1st cycle of $MoSe_2$@C anode at various current densities approach to ca. 60.7%, and increased to above 95% in the subsequent cycles, indicating that the $MoSe_2$@C possesses good reversibility for the desodiation-sodiation.

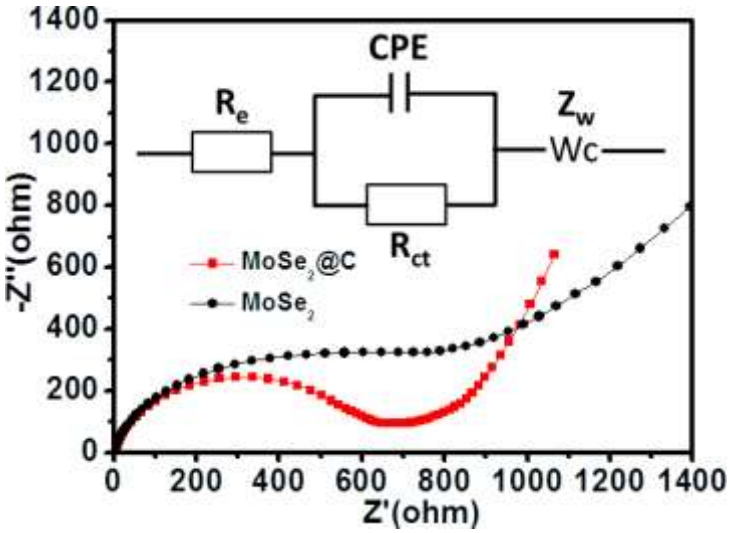

Figure S16. Nyquist plots of the fresh cells and corresponding equivalent circuit model based on $MoSe_2$ and $MoSe_2$@C electrodes in SIBs.

In the equivalent circuit model, the R_e, R_{ct}, Z_w, and CPE represent the ohm resistance of the electrolyte and electrode in high frequency region, charge transfer resistance in middle frequency region, and Warburg impedance related to the ionic diffusion in low frequency region, and double layer capacitance and passivation film capacitance, respectively. The electrochemical impedance spectroscopy (EIS) of the $MoSe_2$ and $MoSe_2$@C electrodes was measured to evaluate their reaction dynamics, in which the smaller semi-cycle located at medium frequency band of the $MoSe_2$@C than that of the $MoSe_2$ suggests the enhanced charge transfer efficiency.

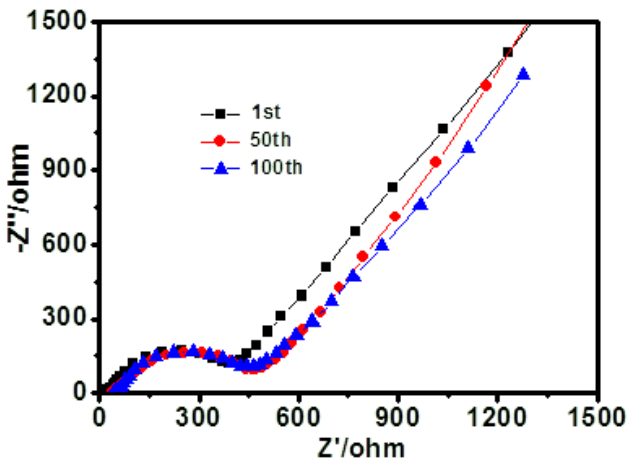

Figure S17. Nyquist plots of $MoSe_2$@C anode in a half cell after various cycles.

After 50th discharge-charge cycle, the semi-cycle located at medium frequency band shows an enlarged charge transfer resistance (R_{ct}) compared to that in 1st cycle. In the subsequent cycles (50th to 100th cycles), however, there is no obvious increase in R_{ct}, suggesting a robust cyclability of $MoSe_2$@C anode.

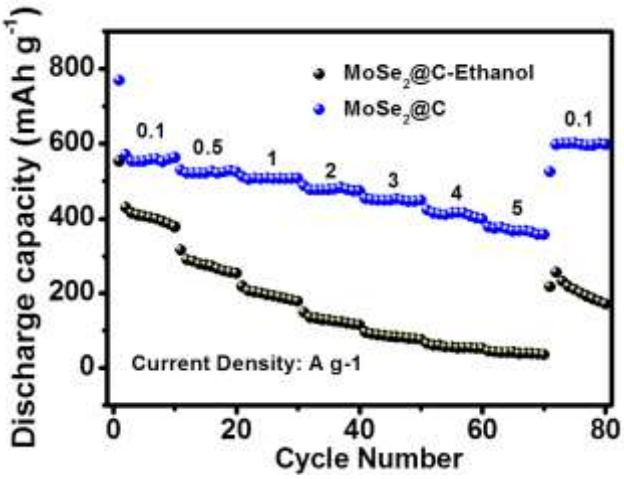

Figure S18. Rate capability of $MoSe_2$@C synthesized with the help of different solvents (oleic acid and ethanol). $MoSe_2$@C and $MoSe_2$@C-Ethanol represent the sample synthesized by using oleic acid and ethanol as solvent, respectively.

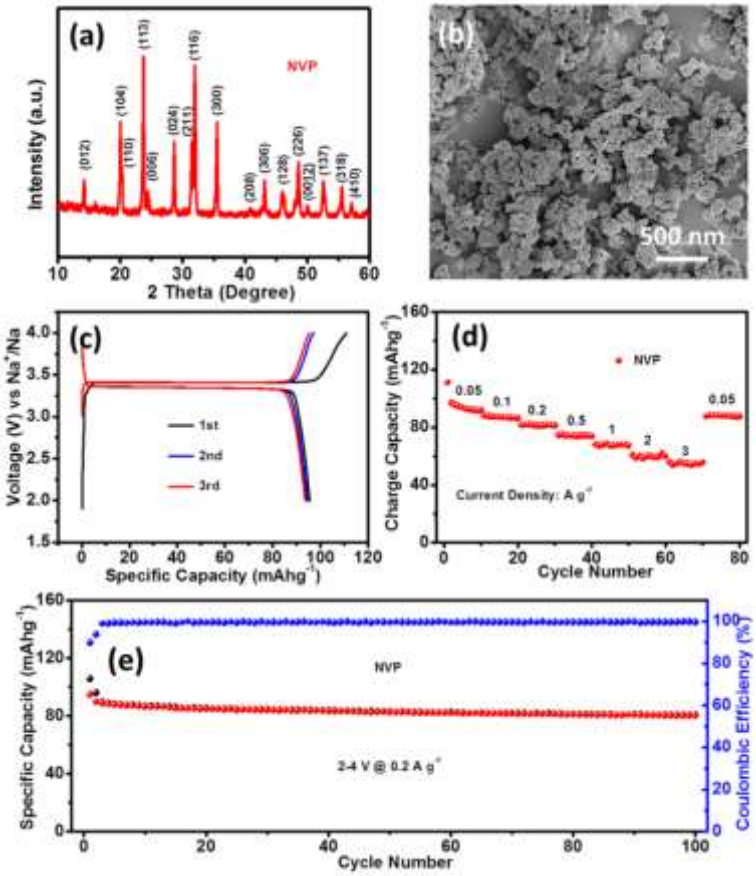

Figure S19. Chemical compositions, morphological features, and electrochemical performance of $Na_3V_2(PO_4)_3$ (NVP). (a) XRD pattern. (b) FE-SEM image. (c)-(e) Electrochemical performance of NVP cathode in sodium ion half batteries.

References

1. Shi, Z.-T.; Kang, W.; Xu, J.; Sun, Y.-W.; Jiang, M.; Ng, T.-W.; Xue, H.-T.; Yu, D. Y. W.; Zhang, W.; Lee, C.-S., Hierarchical Nanotubes Assembled from MoS_2-Carbon Monolayer Sandwiched Superstructure Nanosheets for High-Performance Sodium Ion Batteries. *Nano Energy* **2016,** *22*, 27-37.

2. Xie, X.; Ao, Z.; Su, D.; Zhang, J.; Wang, G., MoS_2/Graphene Composite Anodes with Enhanced Performance for Sodium-Ion Batteries: The Role of the Two-Dimensional Heterointerface. *Adv. Funct. Mater.* **2015,** *25*, 1393-1403.

3. Zhang, K.; Hu, Z.; Liu, X.; Tao, Z.; Chen, J., $FeSe_2$ Microspheres as a High-Performance Anode Material for Na-Ion Batteries. *Adv. Mater.* **2015**, *27*, 3305-3309.

4. Sun, W.; Rui, X.; Yang, D.; Sun, Z.; Li, B.; Zhang, W.; Zong, Y.; Madhavi, S.; Dou, S.; Yan, Q., Two-Dimensional Tin Disulfide Nanosheets for Enhanced Sodium Storage. *ACS Nano* **2015,** *9*, 11371-11381.

5. Choi, S. H.; Ko, Y. N.; Lee, J.-K.; Kang, Y. C., 3D MoS_2-Graphene Microspheres Consisting of Multiple Nanospheres with Superior Sodium Ion Storage Properties. *Adv. Funct. Mater.* **2015,** *25*, 1780-1788.

6. Zhang, Z.; Yang, X.; Fu, Y.; Du, K., Ultrathin Molybdenum Diselenide Nanosheets Anchored on Multi-Walled Carbon Nanotubes as Anode Composites for High Performance Sodium-Ion Batteries. *J. Power Sources* **2015,** *296*, 2-9.